communications biology

A Nature Portfolio journal

Article

https://doi.org/10.1038/s42003-025-08405-0

Molecular mechanism of human α_{1A}-adrenoceptor inhibition by Mamba snake toxin AdTx1

Mingyu Shi[1,2,3,6], Shuhao Zhang[1,3,6], Angqi Zhu[3,4,6], Yosuke Toyoda[2,3], Fang Kong[3,4], Xiaoou Sun[2,3] ✉, Xinyu Xu[1,3] ✉, Chuangye Yan[3,4] ✉ & Xiangyu Liu[1,3,5] ✉

There is growing interest in peptide or small protein based drugs targeting G protein-coupled receptors (GPCRs) for improved subtype selectivity over small molecules. Naturally occurring toxins represent rich sources of such ligands. AdTx1 (ρ-Da1a), a three-finger toxin (3FTx) from the green Mamba Snake, selectively binds and antagonizes α-adrenoceptors. Here, we present the cryo-electron microscopy structure of α_{1A}-adrenoceptor in complex with AdTx1. The structure reveals the molecular mechanism of the subtype selectivity and antagonist activity of AdTx1 for α_{1A}-adrenoceptor, which is different from those revealed by the only 3FTx-GPCR structure reported so far, the Muscarinic toxins 7 (MT7) - Muscarinic acetylcholine receptor 1 (M_1AChR) structure. Based on the structural information, we further engineered the AdTx1 and enhanced its antagonist activity by introducing three mutations. The results highlight the potential of developing potent toxin drugs towards GPCRs based on the 3FTx scaffold and structural information.

G protein-coupled receptors (GPCRs) represent the largest family of transmembrane receptors and regulate a variety of physiological responses. Due to their important physiological roles, GPCRs account for the targets of about one-third of the FDA-approved small-molecule drugs[1]. Drug innovation targeting GPCRs draws extensive attention from both academia and industry. One major challenge in GPCR drug development is to achieve high subtype selectivity because many pharmaceutically important GPCRs have closely related subtypes with high sequence similarity, for example, the nine subtypes of adrenergic receptors in the human genome. Small-molecule drugs have limited interaction interfaces and are difficult to achieve superior subtype selectivity. Peptide or small protein ligands bind to the receptors through larger interaction interfaces and thus have greater potential to be subtype-selective.

One rich source of small protein ligands comes from the venoms produced by toxic animals, such as snakes, spiders, or scorpions[2]. Among these venoms, some exhibit lethal and debilitating effects as a consequence of neurotoxic, cardiotoxic, and tissue-necrotizing effects. However, other venoms exhibit various pharmacological effects with a lower order of toxicity[3]. Many pharmacologically active molecules extracted from these venoms show potential for developing therapeutic agents[4]. For example, bradykinin-potentiating peptides have been used as inhibitors of angiotensin-converting enzyme[5,6], eptifibatide has been used to inhibit platelet aggregation[7,8], tirofiban and ancrod are used to reduce blood fibrinogen levels[9]. Venom toxins also have extensive applications as research tools[10]. For example, α-bungarotoxin has been used to characterize the fundamental mechanisms involved in neuromuscular transmission[11,12].

AdTx1 is a 65-amino-acid peptide toxin isolated from the venom of the green Mamba Snake *Dendrosapis angusticeps*[13]. It functions as an antagonist of the α_{1A}-adrenoceptor (α_{1A}AR) with high selectivity and high affinity[14]. AdTx1 belongs to the 3-finger toxin (3FTx) family, which is characterized by the structures of three-finger loops connected to a central core containing four conserved disulfide bonds[15]. The α_{1A}AR represents one of the nine adrenoceptor subtypes, and its activation mediates smooth muscle contraction. The α_{1A}AR-selective agonist oxymetazoline is clinically used for the treatment of nasal obstruction[16]. The α_{1A}AR antagonists are also clinically used to treat several diseases. For example, tamsulosin and silodosin are used to treat Benign Prostate Hyperplasia (BPH)[17,18]. Doxazosin is used to treat BPH and hypertension[19,20], and prazosin is used to treat overall post-

[1]State Key Laboratory of Membrane Biology, Tsinghua-Peking Center for Life Sciences, School of Pharmaceutical Sciences, Tsinghua University, Beijing, China. [2]School of Medicine, Tsinghua University, Beijing, China. [3]Beijing Frontier Research Center for Biological Structure, Beijing Advanced Innovation Center for Structural Biology, Tsinghua University, Beijing, China. [4]State Key Laboratory of Membrane Biology, Tsinghua-Peking Center for Life Sciences, School of Life Sciences, Tsinghua University, Beijing, China. [5]Beijing Key Laboratory of Cardiovascular Receptors Research, Peking University, Beijing, China. [6]These authors contributed equally: Mingyu Shi, Shuhao Zhang, Angqi Zhu. ✉e-mail: xiaoou@mail.tsinghua.edu.cn; psxlxxy@gmail.com; yancy2019@mail.tsinghua.edu.cn; liu_xy@mail.tsinghua.edu.cn

traumatic stress disorder (PTSD)[21]. We have recently solved the structures of the α_{1A}AR bound with oxymetazoline, tamsulosin, or noradrenaline[22]. However, the detailed interaction pattern between the AdTx1 and α_{1A}AR remains unknown. Exploring the molecular mechanism of how they interact with each other may provide valuable information to guide future peptide drug development. To achieve the research goal, we determined the structure of the AdTx1-α_{1A}AR complex. The structure reveals the molecular mechanism of AdTx1's antagonist activity and provides guidance to engineer AdTx1 based on the structural information. As a proof of concept, we improved the affinity of AdTx1 towards the α_{1A}AR by introducing three mutations to the toxin. The result highlights the possibility of developing and optimizing toxin ligands for GPCRs based on structures.

Results

Complex formation and structure determination of the AdTx1-α_{1A}AR-Nb6

Inspired by the previous work on MT7-M_1AChR structures[23], we tried to recombinantly express AdTx1 in Hi5 insect cells. N-terminal Maltose-binding protein (MBP) fusion was applied to improve the expression level, while MBP was digested and removed during purification (Fig. S1). The purified AdTx1 exhibits high affinity towards the α_{1A}AR as shown by the radioligand competition binding assay. AdTx1 also shows high selectivity towards the α_{1A}AR compared to the α_{1B}AR and α_{1D}AR (Fig. 1a). The results are consistent with previous reports[13]. To further analyze the antagonist activity of AdTx1, we established a cAMP-based GloSensor assay by co-expressing α_{1A}AR with an engineered Gsq protein, which was constructed by replacing 15 residues at the C-terminus of Gαs with those of Gαq[24]. The Gsq protein could be activated by Gq-coupled GPCRs like α_{1A}AR and triggers downstream Gs signaling pathway, such as stimulating cAMP production. As shown in Fig. S3, only HEK293T cells transfected with α_{1A}AR resulted in oxymetazoline-induced cAMP accumulation in the GloSensor cAMP assay, indicating that the response is mediated by the transfected α_{1A}AR receptor, but not the endogenous receptors from the HEK293T cells (Fig. S3). Compared to oxymetazoline, norepinephrine shows a certain level of activation effects on the endogenous receptors of HEK293T. As a result, we chose oxymetazoline in the subsequent functional experiments. The purified AdTx1 shows antagonist activity in inhibiting oxymetazoline-induced cAMP generation (Fig. 2b). Taken together, the recombinantly expressed and purified AdTx1 is functional and suitable for structural studies.

We initially prepared the AdTx1-α_{1A}AR complex and collected cryo-electron microscopy (cryo-EM) data on it. However, cryo-EM data processing was not successful due to the small size and the lack of soluble domains of the complex. We then tried to add fiducial markers to the samples to help particle alignment in cryo-EM data processing. After several trials, we succeeded in applying the previously reported nanobody-6 (Nb6) strategy to help structure determination[25,26]. In brief, we replaced an intracellular loop 3 (ICL3) of α_{1A}AR ($E^{5.68}$ to $K^{6.31}$, superscripts indicate Ballesteros-Weinstein numbering for GPCRs[27]) with that of the κ-opioid receptor (κOR) ($V256^{5.68}$ to $R270^{6.31}$). The resulting α_{1A}AR construct can form a complex with Nb6 through the engineered ICL3. The AdTx1-α_{1A}AR-Nb6 complex was prepared as described in the "Methods" section. The structure of the AdTx1-α_{1A}AR-Nb6 complex was determined by single-particle cryo-EM to a resolution

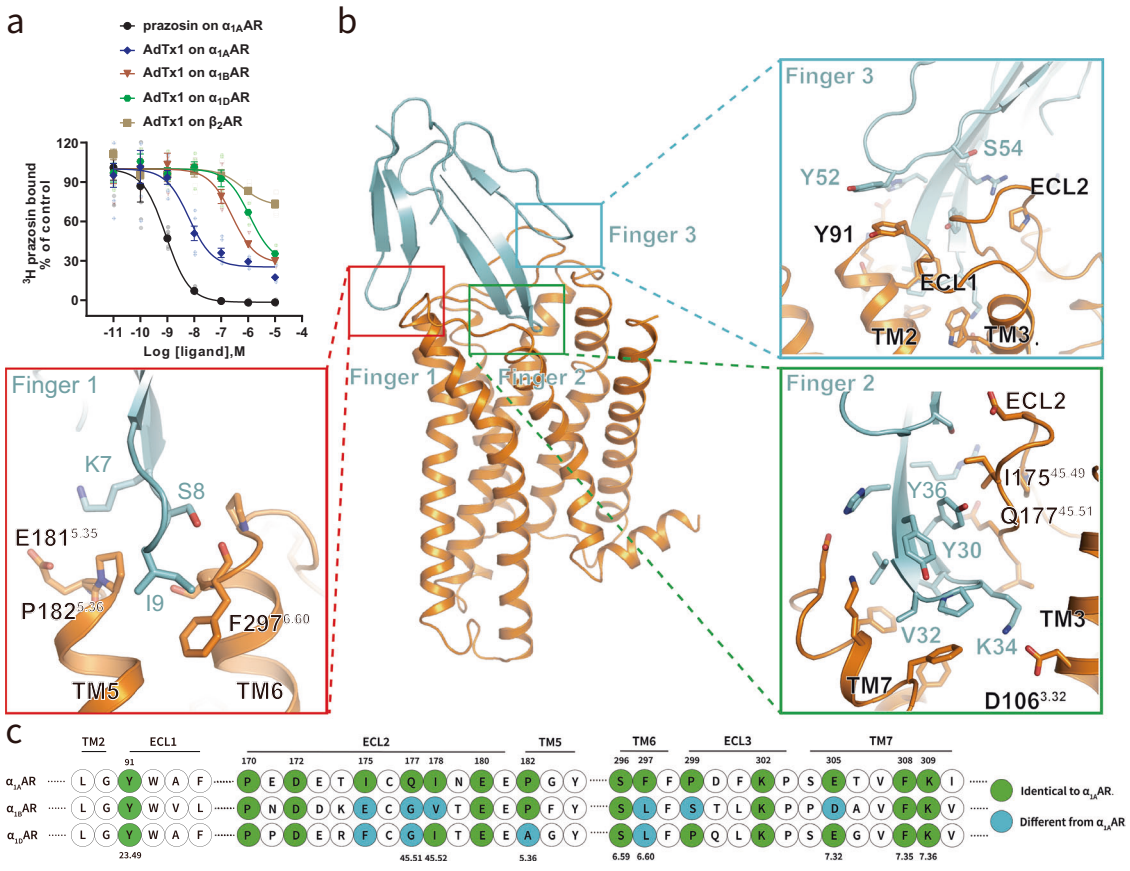

Fig. 1 | Overall structure of the AdTx1-α_{1A}AR-Nb6. a AdTx1 is selective towards the α_{1A}AR over the other subtypes of α_1ARs and β_2AR in a radioligand competition binding assay. Data are given as means ± SEM of 6 independent samples. **b** AdTx1 binds to the extracellular side of the α_{1A}AR, with finger loop 1 interacting with the extracellular end of TM5 and TM6 (red square), finger loop 2 binds to the central cavity (green square), and finger loop 3 contacts the ECL1 (cyan square). **c** Sequence alignment of the extracellular regions of α_1ARs. The α_{1A}AR residues that interact with AdTx1 are colored in green. The residues on the α_{1B}AR or α_{1D}AR are also colored in green if they are identical to those of the α_{1A}AR, non-conserved residues are colored in cyan.

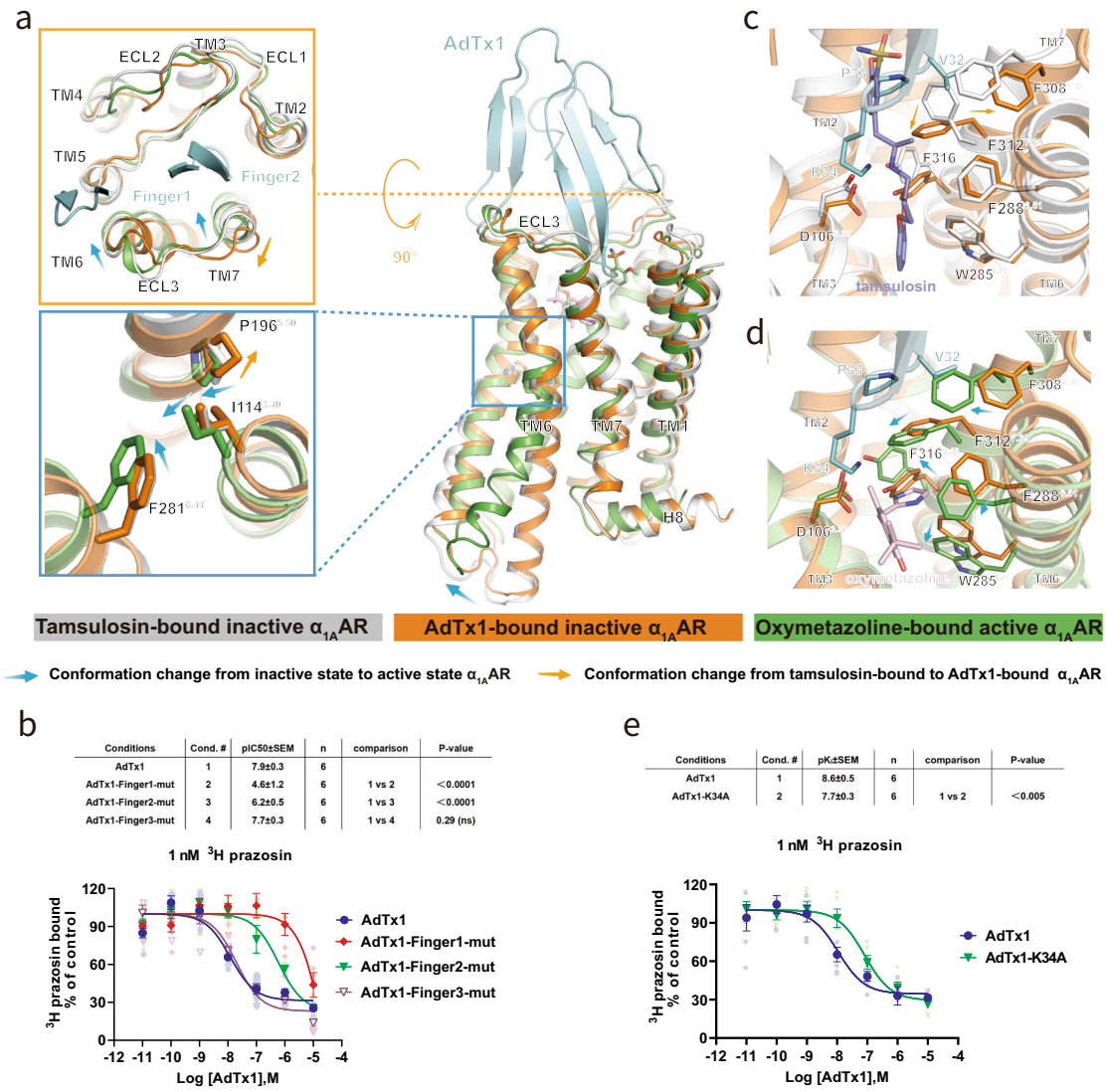

Conditions	Cond. #	pIC50±SEM	n	comparison	P-value
AdTx1	1	7.9±0.3	6		
AdTx1-Finger1-mut	2	4.6±1.2	6	1 vs 2	<0.0001
AdTx1-Finger2-mut	3	6.2±0.5	6	1 vs 3	<0.0001
AdTx1-Finger3-mut	4	7.7±0.3	6	1 vs 4	0.29 (ns)

Conditions	Cond. #	pK±SEM	n	comparison	P-value
AdTx1	1	8.6±0.5	6		
AdTx1-K34A	2	7.7±0.3	6	1 vs 2	<0.005

Fig. 2 | Molecular mechanism of AdTx1's antagonist activity. a Structure comparison of the AdTx1-bound α_{1A}AR structure (orange) with the tamsulosin-bound inactive state α_{1A}AR structure (gray, PDB code: 7YMJ) and the oxymetazoline-bound active state α_{1A}AR structure (green, PDB code: 7YM8). Finger loop 1 and finger loop 2 of AdTx1 prevent the inward movement of TM6 and TM7, which are required for the α_{1A}AR activation (orange rectangle). AdTx1 binding causes a more outward conformation of TM7 (orange arrow) and stabilizes the PIF motif at the inactive conformation (cyan rectangle). **b** Mutating finger loop 1 (K7A, S8A, and I9A) has the largest effect on AdTx1 function in a ^{3}H prazosin competition binding assay, mutating finger loop 2 (Y30A, V32A, and K34A) also reduced AdTx1 function, while mutating finger loop 3 (Y52A and S54A) does not have much effect on AdTx1 function. Data are given as means ± SEM of 6 independent samples. **c** Compared to tamsulosin-bound inactive α_{1A}AR, conformational changes of F308$^{7.35}$, F312$^{7.39}$ are observed upon AdTx1 binding. **d** K34 at the finger loop 2 of AdTx1 directly interacts with D106$^{3.32}$ and distorts the conformation of D106$^{3.32}$, thus altering the shape of the orthosteric pocket of α_{1A}AR. V32 at the finger loop 2 of AdTx1 extrudes the F308$^{7.35}$, leading to the outward movement of TMs 6 and 7 of α_{1A}AR. Compared to the oxymetazoline-bound active α_{1A}AR, conformational changes of F288$^{6.51}$, F308$^{7.35}$, F312$^{7.39}$, and W285$^{6.48}$ are observed upon AdTx1 binding. **e** K34A mutation impairs the function of AdTx1 in a ^{3}H prazosin competition binding assay. Data are given as means ± SEM of 6 independent samples.

of 2.87 Å (Fig. S4, Table 1). The electron densities are clear enough to model most of the receptor, AdTx1 and Nb6, except for the N-terminal region (M1 to I23) and C-terminal region (Q344 to Q370) of the α_{1A}AR, as well as the C-terminal region of Nb6 (120–125) due to poor densities that are likely resulted from flexibility.

Overall structure

AdTx1 binds to the extracellular side of the α_{1A}AR while Nb6 binds to the engineered ICL3 as designed (Fig. S5a). Since the Nb6 binding site is far away from the AdTx1 binding site, it was omitted from the main figures for clarity. As mentioned earlier, the AdTx1 is composed of 6 beta-strains that form 3-finger loops. The finger loop 2 penetrates deep into the central cavity of the receptor which is also the path towards the orthosteric pocket, while finger loop 1 interacts with transmembrane helices (TMs) 5 and 6 and finger loop 3 interacts with extracellular loops (ECLs) 1 and 2 (Fig. 1b). The structure is in agreement with previous mutagenesis studies, where mutations of orthosteric residues F86$^{2.64}$A, E87$^{2.65}$A, D106$^{3.32}$A, F288$^{6.51}$A, and F312$^{7.39}$A significantly affect the affinity between AdTx1 and the α_{1A}AR[2,14]. Of the 15 residues that form the AdTx1 binding site on the α_{1A}AR, 9 of them are different in the α_{1B}AR and 11 are different in α_{1D}AR (Fig. 1c). According to the radioligand competition results and previous publications[13], AdTx1 is selective towards the α_{1A}AR over the other subtypes of α_1ARs. (Fig. 1a). The interface differences may explain the selectivity of AdTx1 towards the different α_1ARs.

Molecular mechanism of antagonist activity of AdTx1

In order to understand the molecular mechanism of AdTx1's antagonist activity towards the α_{1A}AR, we compared the AdTx1-bound

Table 1 | Cryo-EM data collection, refinement, and validation statistics

	AdTx1-α_{1A}AR-Nb6 (EMDB-34906) (PDB 8HN1)
Data collection and processing	
Microscope	Titan Krios G3i
Detector	Gatan K3
Magnification	81,000
Voltage (kV)	300
Electron exposure (e–/Å^2)	50
Defocus range (μm)	−1.3~−1.8
Pixel size (Å)	1.083
Symmetry imposed	C1
Initial particle images (no.)	4579 k
Final particle images (no.)	617 k
Map resolution (Å)	2.87
FSC threshold	0.143
Map resolution range (Å)	50~2.4
Refinement and validation	
Initial model used (PDB code)	α_{1A}AR: inactive α_{1A}AR model bound to tamsulosin: 7YMJ AdTx1: 4IYE Nb6: 6VI4
Model resolution (Å)	2.87
FSC threshold	0.143
Map sharpening *B* factor (Å^2)	−154.2
Model composition	
Non-hydrogen atoms	3560
Protein residues	458
B factors (Å^2)	
Protein	27.87/163.91/70.18
R.m.s. deviations	
Bond lengths (Å)	0.003
Bond angles (°)	0.578
Validation	
MolProbity score	1.70
Clashscore	7.72
Poor rotamers (%)	0.00
Ramachandran plot	
Favored (%)	95.98
Allowed (%)	4.02
Disallowed (%)	0.00

α_{1A}AR structure with both the oxymetazoline-bound active state of α_{1A}AR and the tamsulosin-bound inactive state of α_{1A}AR (Fig. 2a)[22]. A hallmark of GPCR activation is the outward displacement of the intracellular side of TM6. The AdTx1-bound α_{1A}AR is in inactive conformation as expected (Fig. 2a). The conformation of TM6 is similar to that of the tamsulosin-bound α_{1A}AR structure. A close analysis of the extracellular side of the receptor conformation reveals that the extracellular sides of the TM6 and TM7 display inward movement upon receptor activation (Fig. 2a, orange rectangle), which then induces conformational change through the PIF motif (Fig. 2a, blue rectangle) and result in the outward displacement of the intracellular side of TM6[22]. The finger loop 1 of AdTx1 inserts between TM5 and TM6, while the finger loop 2 of AdTx1 inserts between TM7 and ECL2 (Fig. 2a, orange rectangle), thus preventing the inward movement of TM6 and TM7 and locking the receptor in an inactive conformation. Actually, in the AdTx1-bound structure, the extracellular part of TM7 is stabilized in an even more outward conformation by the finger loop 2 compared to the tamsulosin-bound structure (Fig. 2a, orange rectangle). The hydrophobic residue V32 of AdTx1 extrudes F308$^{7.35}$, leading to the outward movement of TMs 6 and 7 of α_{1A}AR (Fig. 2c, d). When compared with the tamsulosin-bound inactive α_{1A}AR structure, F308$^{7.35}$ and F312$^{7.39}$ are in a more outward conformation, while tamsulosin induces an open-lid conformation of F312$^{7.39}$ (Fig. 2c). Compared to the oxymetazoline-bound active α_{1A}AR, conformational changes of F288$^{6.51}$, F308$^{7.35}$, F312$^{7.39}$, as well as the toggle-switch W285$^{6.48}$, are observed upon AdTx1 binding (Fig. 2d).

Previous mutagenesis studies have pinpointed key residues on each of the three-finger loops that play a critical role in the interaction between the toxin and the receptor[2,28]. These findings are consistent with the structural data. For instance, K7 from finger loop 1 is shown to engage in an interaction with E181^{ECL2} (Fig. 1b), the K7A mutation leads to a 5-fold decrease in binding affinity compared to wild-type toxin[2]. An intriguing observation was made with F10 also on Finger loop 1. Despite not having direct contact with the receptor, the F10A mutation resulted in an even more dramatic loss of affinity—approximately 18-fold lower than the native toxin[2]. This suggests that maintaining a hydrophobic microenvironment around finger loop 1 and its proximity to TM5/6 are essential for the stability of the toxin-receptor complex. This highlights the indirect yet significant role played by non-contacting residues in stabilizing the overall structure and orientation of the toxin, thereby influencing its binding efficiency. The structural data indicates that S8 interacts with the main chain carbonyl oxygen of F297$^{6.60}$, while the side chain of I9 interacts with the benzene ring of F297$^{6.60}$ (Fig. 1b), a combination of K7A/S8A/I9A triple mutation leads to a dramatic decrease in the toxin's affinity for the receptor, estimated to be approximately 2000-fold lower than that of the wild-type toxin (Fig. 2b). This is noteworthy when compared to the relatively less severe impact of the single K7A mutation which only caused a reduction in affinity by around 5-fold[2,28]. Y36 from finger loop 2 forms extensive interactions with ECL2 residues I175^{ECL2} and Q177^{ECL2} (Fig. 1b), the Y36A mutation results in a dramatic 1900-fold decrease in Ki value, highlighting the importance of the interaction[2,28]. Interestingly, in finger loop 3, only the sidechains of Y52 and S54 are within 4 Å distance of the receptor, while the Y52A/S54A double mutation has similar affinity towards the receptor as the wild-type AdTx1 (Fig. 2b). On the contrary, the D53A single mutation reduced the affinity by 53-fold[2,28]. Structure information suggests D53, H29, and E305$^{7.32}$ form a hydrogen bond network (Fig. S7). The results indicate that the direct interactions between finger loop 3 of the toxin and the receptor itself do not significantly contribute to the functional potency of the toxin. Instead, finger loop 3 plays a crucial role in maintaining the structural integrity and proper conformation of finger loop 2.

The finger loop 2 penetrates deep into the orthosteric pocket and forms a salt bridge with D106$^{3.32}$ through K34 (Fig. 2c). D106$^{3.32}$ is a highly conserved residue among the aminergic receptors, and its negatively charged side chain is important for aminergic ligands binding[29,30], including adrenergic receptors, dopamine receptors, and serotonin receptors[31–34]. Previous active and inactive α_{1A}AR structures reveal that both the agonists (norepinephrine and oxymetazoline) and antagonist (tamsulosin) form polar interactions with D106$^{3.32}$ [22]. Similar polar interactions also exist in other aminergic receptors (Fig. S8). The interaction between K34 and D106$^{3.32}$ distorts the conformation of D106$^{3.32}$ and alters the shape of the orthosteric pocket of α_{1A}AR (Fig. 1b, green rectangle), thus affecting the interaction between α_{1A}AR and its orthosteric ligands (Fig. 2c). Previous studies suggest the D106$^{3.32}$A mutation resulted in reduced AdTx1 affinity[14]. Notably, the K34A single mutation also reduces AdTx1's affinity towards the α_{1A}AR (Fig. 2e), as well as its antagonist activity in inhibiting oxymetazoline-induced cAMP generation in the α_{1A}AR-Gsq GloSensor cAMP assay (Fig. S6).

Structure-based engineering improves the affinity of AdTx1 to α_{1A}AR

We further explored whether it's possible to improve the antagonist activity of AdTx1 based on the structural information. As described before, the salt bridge between K34 of AdTx1 and D106$^{3.32}$ of a_{1A}AR affects the shape of the orthosteric pocket and thus affects orthosteric ligand binding (Fig. 2c). We replaced K34 with arginine and found the K34R mutant shows enhanced activity compared to the wild-type AdTx1 (Fig. S9). Similarly, we mutated H29 on finger loop 2 into arginine (H29R) to enhance its interaction with E305$^{7.32}$ and mutated S54 on finger loop 3 into glutamine (S54Q) or asparagine (S54N), to form hydrogen bonds between R28 of AdTx1 and D172^{ECL2} of α_{1A}AR (Fig. 3a). The H29R and S54Q mutants also enhance inhibitory function compared to the wild-type AdTx1 (Fig. S9), while S54N shows impaired function, most likely suggesting that the asparagine side chain is not long enough to induce the proper hydrogen bonds formation between R28 and D172^{ECL2} (Fig. S9). We further generated a triple mutation of AdTx1 (AdTx1-3mut) by combining all three mutations H29R, K34R, and S54Q. While the AdTx1-3mut only shows 5-fold higher affinity than the WT AdTx1 in radioligand competition binding assay (Fig. 3b), it exhibits 12-fold higher potency in inhibiting oxymetazoline-induced receptor activation (Fig. 3c). The results highlight the possibility to engineer and improve toxin activity based on the structural information.

Comparison of the AdTx1- α_{1A}AR structure with the MT7-M_1AChR structure

Previously, only one GPCR-snake toxin complex was reported, which is the MT7-M_1AChR complex structure[23]. MT7 and AdTx1 share 68% sequence identity and the 3FTx scaffold[13]. We then compared the binding mode of MT7 for M_1AChR against that of AdTx1 for α_{1A}AR (Fig. S10). The most obvious difference is that AdTx1 binds to a deeper position than the MT7 (Fig. 4a–c). Consistent with the binding mode difference, MT7 functions as a negative allosteric modulator for the M_1AChR activation and does not directly compete with orthosteric ligands[23]. In contrast, AdTx1 distorts the orthosteric ligand binding by the salt bridge between K34 and D106$^{3.32}$ (Fig. 4c). Besides, the binding poses of MT7 and AdTx1 are shifted by around 50 degrees (Fig. 4d). While finger loop 2 of both toxins insert to the extracellular cavities of the receptors formed by ECL2, ECL3 and TM7, the finger loop 1 and 3 of AdTx1 bind to different regions of the receptor compared to the MT7. The finger loop 1 of MT7 is inserted between TM4 and TM5 of M_1AChR, while finger loop 1 of AdTx1 is inserted between TM5 and TM6 of α_{1A}AR. Finger loops 3 of MT7 interacts with TM7 of M_1AChR, while finger loop 3 of AdTx1 interacts with ECL1 of α_{1A}AR (Fig. 4d). However, even though AdTx1 inserts deeper than MT7, our radioligand competition assay shows that AdTx1 cannot fully displace prazosin, even at a concentration up to ten-thousand fold higher than that of prazosin (Fig. S11). This suggests the possible existence of an alternative state in which AdTx1 and prazosin may coexist, indicating a more complex binding mode than captured by our structure. These findings highlight the diversity of possible interaction patterns between 3FTxs and GPCRs.

Discussion

Snakes, particularly those that rely on venom to capture prey, exhibit remarkable ecological adaptability and a diverse range of hunting strategies. These efficient predators can target a wide array of species, ranging from small mammals to birds and even other reptiles, using their venom to swiftly subdue their prey, thereby ensuring effective energy acquisition. Our high-resolution cryo-EM structure elucidates the detailed mechanism of one such venom component, AdTx1, targeting the α_{1A}AR. Despite variations in the receptor protein sequences across different species, the AdTx1 binding site remains highly conserved, from small mammals such as mice and rabbits, through birds like the wall lizard (Podarcis muralis), to other reptiles including the pied flycatcher (Ficedula albicollis) (Fig. S12). This conservation highlights the effectiveness of AdTx1 in targeting multiple species. The highly conserved AdTx1 binding site on the receptor also indicates a conserved evolutionary pressure acting upon this binding site.

The structural complementarity of AdTx1 to the α_{1A}AR's extracellular vestibule is remarkable, suggesting an evolutionary fit for these toxins to their targets. This fit is not merely a consequence of size but also the spatial arrangement of key residues that mediate the antagonistic effect. The finger loops of the 3FTx scaffold, particularly loop 2, appear to be tuned for effective receptor binding and inhibition, as demonstrated by our mutagenesis experiments. The comparison between the AdTx1-α_{1A}AR complex with the MT7-M1AChR structure reveals the adaptability of the 3FTx scaffold. It shows how subtle shifts in the binding pose can result in diverse mechanisms of receptor modulation, from negative allosteric modulation to direct competitive inhibition. One interesting observation is that the positively charged residues on finger loop 2, K34 in AdTx1 and R34 in MT7, play a key role in interacting with the receptor. This interaction highlights the importance of electrostatic complementarity between the toxin and the receptor. The specific positioning of these charged residues not only facilitates the initial encounter but also stabilizes the toxin-receptor complex, contributing to the high affinity and selectivity observed.

A comparison of the structures of AdTx1 bound to the α_{1A}AR and cyclazocine bound to the α_{1B}AR reveals overall similar conformation but differences in the extracellular regions of the receptors (Fig. S13). The TM2 displays more outward displacement in the α_{1B}AR compared to α_{1A}AR. In addition, the distinct orientations of ECL1 and ECL2 in the α_{1A}AR versus the α_{1B}AR contribute to the varying affinities of AdTx1 for these two receptors (Fig. S13). This observation aligns with the lower affinity of AdTx1 for the α_{1B}AR, as demonstrated experimentally (Fig. 1a).

Through the strategic introduction of specific mutations, our research has successfully enhanced the antagonist activity of AdTx1, effectively creating a blueprint for the design and development of optimized toxin-based pharmaceuticals. The triple mutant variant, AdTx1-3mut, serves as a testament to this strategy's feasibility, showcasing improved potency in its interaction with the α_{1A}AR. The strategy is likely generally applicable to other GPCRs. By refining the structure and function of venom-derived peptides, we can potentially develop targeted therapies that more precisely modulate GPCR activity, thereby offering safer and more effective treatments for patients. Looking ahead, the high-resolution structural data obtained from our study provides a robust platform for computational screening and rational design of peptide libraries. This strategy has the potential to significantly expedite the identification of novel ligands with exceptional specificity and affinity for G protein-coupled receptors (GPCRs) that are of clinical importance.

The pursuit of achieving high specificity and selectivity in drug discovery, particularly within the realm of GPCR-targeted therapeutics, remains an arduous task. Our research makes a stride forward in this area by unraveling the inhibitory and selective interaction mechanism through which the Mamba snake toxin AdTx1 interacts with the human α_{1A}AR. Peptides or small proteins like AdTx1 exhibit an inherent structural advantage due to their conformational specificity, which empowers them with an enhanced ability to discriminate between GPCR subtypes. This property is particularly advantageous when aiming at receptors that have closely related variants, where conventional small-molecule drugs often lack the necessary precision.

It is noteworthy that AdTx1 has been characterized as an insurmountable antagonist, meaning that once bound, it cannot be displaced by agonists or other antagonists. This characteristic is closely tied to its mode of action, which involves a tight and stable interaction with the receptor. The insurmountable nature of AdTx1 suggests that its binding involves covalent or highly stable non-covalent interactions that prevent displacement. This property is significant because it ensures that the receptor remains inactive for extended periods. The detailed mechanism of the insurmountable nature of AdTx1, however, is not revealed with the current structure and requires further study. In conclusion, the structural and functional data presented here not only shed light on the evolutionary adaptations of AdTx1 but also

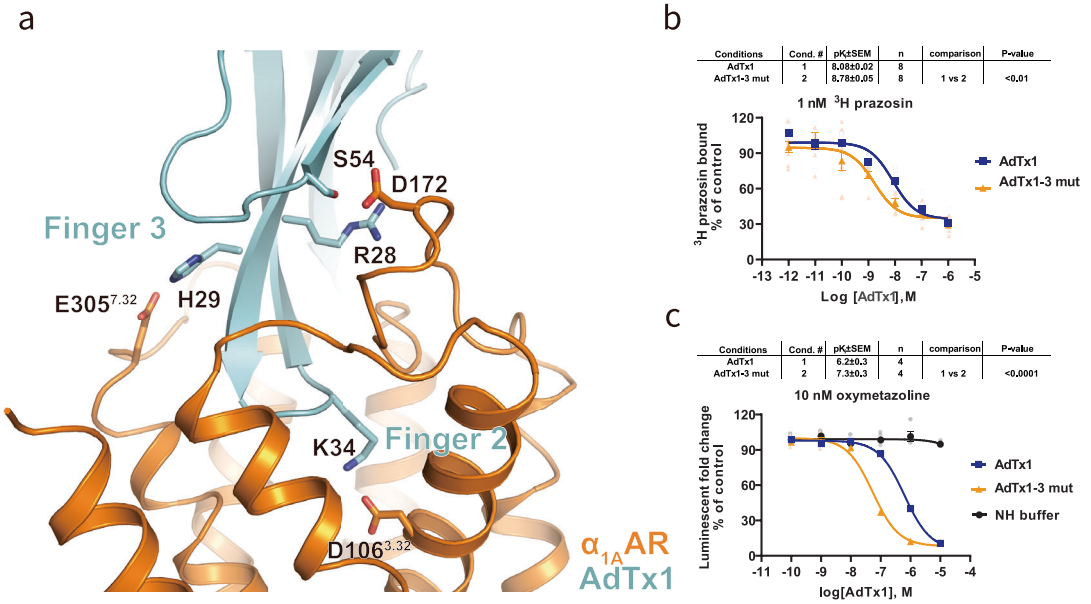

Fig. 3 | Structure-based protein engineering improves the affinity of AdTx1 to α_{1A}AR. a H29 and K34 are chosen for mutation to increase their interactions with E305$^{7.32}$ and D106$^{3.32}$. S54 is chosen to be mutated to either N or Q to bridge the interaction between R28 and D172^{ECL2}. **b** The AdTx1-3mut (H29R, K34R and S54Q) show higher affinity than AdTx1 in a ^{3}H prazosin competition binding assay. Data are given as means ± SEM of 8 independent samples. **c** The AdTx1-3mut shows increased activity in an α_{1A}AR-Gsq cAMP accumulation assay compared to AdTx1. Data as given as means ± SEM of 4 independent samples.

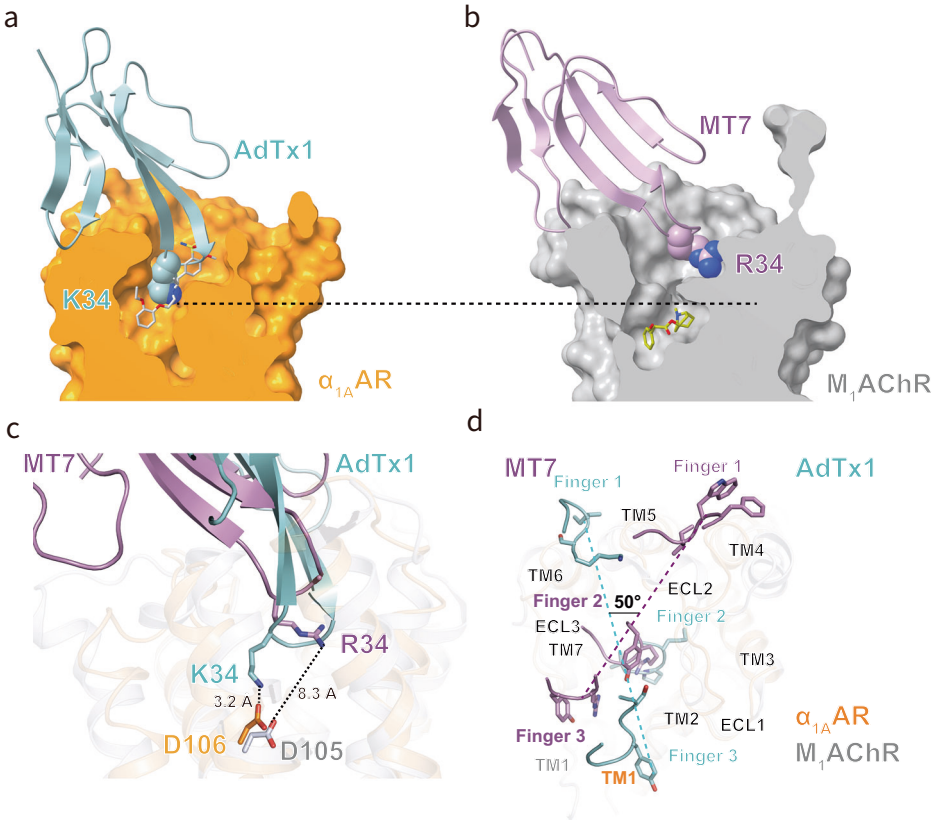

Fig. 4 | Comparison of the structure of AdTx1-α_{1A}AR complex with MT7-M_1AChR complex. **a**, **b** AdTx1 binds to a deeper position in the α_{1A}AR (**a**) compared to MT7 in the M_1AChR (PDB code: 6WJC) (**b**). White and yellow sticks indicate tamsulosin from inactive α_{1A}AR (PDB code: 7YMJ) and atropine from MT7-M_1AChR (PDB code: 6WJC). **c** K34 of AdTx1 directly interacts with D106$^{3.32}$ of the α_{1A}AR while R34 of MT7 is far away from D105$^{3.32}$ of the M_1AChR. **d** A top view comparison of the two structures reveals that the binding poses of MT7 and AdTx1 are shifted by around 50 degrees.

highlight the potential of 3FTx scaffolds as a platform for the development of novel, highly selective GPCR-targeted therapeutics. The insights gained from studying AdTx1's interaction with the α_{1A}AR may pave the way for innovative drug designs aimed at improving therapeutic outcomes while minimizing side effects.

Materials and methods

AdTx1 construct design

The AdTx1 gene was synthesized by GENEWIZ. The final expression construct contains a N-terminal GP64 signal peptide, followed in order by 6 × His tag, MBP, GS-linker, HRV 3C site, GS-linker, and AdTx1 (Fig. S1a).

The construct was cloned into the multiple cloning sites of the pFastBac vector. AdTx1 mutants were generated using site-directed mutagenesis.

AdTx1 expression and purification

The plasmids encoding the WT AdTx1 and AdTx1 mutants were transformed into DH10Bac competent cells, and viruses were prepared following the manual of the Bac-to-Bac® TOPO® Expression System (Invitrogen). Protein expression was performed by adding 30 mL P2 virus to 1 liter of Hi5 cells (Thermo Fisher) with a density of 4×10^6 cells/mL. After 48 h, the transfected Hi5 cells were centrifuged at 4 °C, 4000 rpm for 20 min, and the supernatant was harvested for protein purification. After adding 50 mM Tris-HCl pH = 7.5, 1 mM $NiCl_2$, 5 mM $CaCl_2$, 160 μg/mL benzamidine, and 100 μg/mL leupeptin to the supernatant, the mixture was stirred at room temperature for 1 h and then centrifuged at 14,000 rpm for 30 min at 4 °C to remove metal chelators in the cell culture medium. The resulting supernatant was then applied for Ni-NTA purification. The eluate from the first Ni-NTA column was digested by 3C-protease at room temperature for 1 h followed by 4 °C overnight. The digested protein was then applied to a second Ni-NTA column. The flowthrough of the second Ni-NTA column was collected, concentrated, and purified with a size exclusion chromatography (SEC) Superdex 75 column (Cytica) in a SEC buffer (20 mM HEPES, pH = 7.5, 100 mM NaCl) (Fig. S1c). The SEC peak was checked by SDS-PAGE, and the targeted AdTx1 fraction was collected, concentrated and stored at -80 °C for further use. The expression construct sequence is shown in Fig. S1b. The protein concentration was measured using a Nanodrop (Thermo).

α_{1A}AR construct design

The glycosylation sites (N7, N13, N22) of human α_{1A}AR were mutated to glutamine. A hemagglutinin signal peptide and a FLAG tag were added to the N-terminal of the receptor, and the C-terminus of α_{1A}AR was truncated at residue 370 (full length 466) followed by an 8 × His tag. The ICL3 of the α_{1A}AR ($E^{5.68}$ to $K^{6.31}$) was replaced with that of the κOR ($V256^{5.68}$ to $R270^{6.31}$) to create a Nb6 recognition site[26]. In addition, two mutations $S113R^{3.39}$ and $M115W^{3.41}$, which are reported to stabilize the inactive state or improve receptor expression for other GPCRs[22,35–37], are introduced to the α_{1A}AR. This construct was subcloned to the pFastBac vector.

α_{1A}AR expression and purification

The baculoviruses encoding the α_{1A}AR expression construct were prepared in the same way as previously described for AdTx1 expression. The α_{1A}AR expression was performed by adding 30 mL P2 viruses to each liter of sf9 cells (Expression Systems) with a density of 4×10^6 cells/mL. After 48 h, the transfected sf9 cells were harvested by centrifuging at 4 °C, 4000 rpm for 20 min.

The cell pellets were lysed in lysis buffer containing 20 mM Tris-HCl pH = 7.5, 1 mM EDTA, 160 μg/ml benzamidine, and 100 μg/ml leupeptin for 15 min at 4 °C. After centrifuging at 18,000 rpm for 10 min at 4 °C, the pellet was solubilized in solubilization buffer containing 20 mM HEPES pH = 7.5, 0.03% cholesterol hemisuccinate (CHS), 1% dodecyl maltoside (DDM), 750 mM NaCl, and 30% glycerol for 2 h. 2 mg/ml iodoacetamide was added to the solubilization buffer. 1 mL/L Ni-NTA beads were added to the mixture. After stirring for 2 h at 4 °C, the receptors were eluted with elution buffer containing 20 mM HEPES pH = 7.5, 0.03% CHS, 0.1% DDM, 750 mM NaCl and 200 mM imidazole. The eluate was supplemented with 2 mM $CaCl_2$ and loaded onto the M1 column. The detergents were gradually changed from DDM to 0.01% Lauryl Maltose Neopentyl Glycol (LMNG) on the M1 column. Finally, the α_{1A}AR receptors were eluted from M1 beads with elution buffer containing 20 mM HEPES pH = 7.5, 0.01% MNG, 0.001% CHS, 100 mM NaCl, 0.2 mg/ml Flag peptide, and 5 mM EDTA. The M1 column eluate was then concentrated and purified with a size exclusion chromatography (SEC) Superdex 200 increase column (Cytica) in SEC buffer comprised of 20 mM HEPES pH =7 .5, 0.01% MNG, 0.001% CHS, and 100 mM NaCl (Fig. S2). The SEC peak containing the receptor was then concentrated, flash-frozen in liquid nitrogen, and stored at −80 °C for further use.

Nb6 expression and purification

The Nb6 gene was synthesized by GENEWIZ and subcloned into the periplasmic expression vector pET22b. The expression construct contains a N-terminal signal peptide and a C-terminal 8 × His tag. The expression plasmids were transformed into BL21(DE3) *E. coli*. Protein expression was induced with 1 mM IPTG when the cells were grown to OD = 0.8, and cell pellets were harvested after expression for 20 h at 20 °C. Nb6 purification was performed as previously described. Briefly, pellets were resuspended in SET buffer (200 mM Tris, pH 8.0, 500 mM sucrose, 0.5 mM EDTA) and rotated at 4 °C for 1 h. Then, a 2 × volume of SET/4 buffer (50 mM Tris, pH 8.0, 125 mM sucrose, 0.125 mM EDTA) was added, and the mixture was stirred at room temperature for another hour. After centrifugation at 18,000 rpm, the supernatant was loaded onto Ni-NTA beads. Following washes with high salt buffer (20 mM Tris, pH 8.0, 500 mM NaCl, 20 mM imidazole) and low salt buffer (20 mM Tris, pH 8.0, 100 mM NaCl, 20 mM imidazole), the Nb6 was eluted with elution buffer (20 mM Tris, pH 8.0, 100 mM NaCl, 200 mM imidazole). The eluted Nb6 was further purified using a size exclusion chromatography (SEC) Superdex 75 increase column (Cytica) equilibrated with 20 mM HEPES-NaOH, pH 7.50, and 100 mM NaCl. The purified nanobodies were stored at −80 °C for further use (Fig. S2).

AdTx1-α_{1A}AR-Nb6 complex formation

The purified α_{1A}AR, AdTx1, and Nb6 were mixed in a molar ratio of 1:1.2:1.2 and incubated on ice for 1 h, and then purified by M1 affinity resin. The complex was eluted from the M1 resin with an elution buffer containing 20 mM HEPES pH = 7.5, 0.002% MNG, 0.0002% CHS and 100 mM NaCl, 0.2 mg/ml Flag peptide, and 5 mM EDTA. The eluate was concentrated and purified with a size exclusion chromatography (SEC) Superdex 200 increase column (Cytica) in SEC buffer comprised of 20 mM HEPES pH = 7.5, 0.002% MNG, 0.0002% CHS, and 100 mM NaCl (Fig. S2). The fraction containing the complex was concentrated to 5 mg/mL and used for cryo-EM sample preparation.

Cryo-EM sample preparation and data collection

4 μL of the purified AdTx1-α_{1A}AR-Nb6 complex was added to glow-discharged holey carbon grids (Quantifoil Au R1.2/1.3, 300 mesh). The grids were blotted for 3.0 s and flash-frozen in liquid ethane cooled by liquid nitrogen with Vitrobot (Mark IV, Thermo Fisher Scientific).

The cryo-EM data were collected at the National Protein Science Research (Beijing) Facility, Tsinghua Base. The grids were transferred to a 300 kV Titan Krios G3i microscope equipped with Gatan K3 Summit detector and a GIF Quantum energy filter (slit width 20 eV). 2,049 movie stacks were collected by using the AutoEMation program[38], with a defocus range from −1.3 μm to −1.8 μm. Each stack contained 32 frames and was exposed for 2.56 s. The total dose of each stack was about 50 $e^-/Å^2$. All 32 frames in each stack were aligned and summed using the whole-image motion correction program MotionCor2 and binned to a pixel size of 1.083 Å[39].

Cryo-EM data processing

The following processes were performed using cryoSPARC 3.2[40]. 2,049 dose-weighted micrographs were imported into cryoSPARC, and CTF parameters were estimated by using patch-CTF. Micrographs with a CTF fitting resolution worse than 4 Å were deleted, resulting in 2025 micrographs for further data processing. 4,578,926 particles were picked by the template picker and extracted. After four rounds of 2D classification, 115,477 particles showed clear features of Nb6, α_{1A}AR, and AdTx1. These particles were selected to generate the initial model by Ab-Initio Reconstruction. By using this initial model, the full set of particles was subjected to 3 rounds of heterogeneous refinement, resulting in a 3.45 Å map

reconstructed by 616,710 particles. Followed by non-uniform refinement and local refinement, the final map reached a resolution of 2.87 Å.

The atomic coordinates of the AdTx1-α_{1A}AR-Nb6 complex were generated by combining homology modeling (PDB code: 4IYE) and the previous α_{1A}AR-Nb6 model (PDB code: 7YMJ). The cryo-EM model was docked with the density map through UCSF Chimera[41]. The structure model was then refined through iterative manual building and refinement in PHENIX[42] and COOT[43]. Figures were prepared using the PyMOL Molecular Graphics System v.2.4.1 (Schrödinger, LLC), UCSF Chimera, and UCSF Chimera X1.3[44].

Radioligand competition binding assay

The wild-type α_{1A}AR, α_{1B}AR, α_{1D}AR, and β_2AR genes were cloned and expressed in the same way as described for AdTx1 previously. Cell membrane extraction and radioligand binding were performed as previously reported[45,46]. In brief, 50 mL of cells expressing the corresponding receptors were harvested and resuspended in 8 mL of lysis buffer containing 20 mM Tris pH 7.5, 1 mM EDTA, 100 μg/ml leupeptin, and 160 μg/ml benzamidine. Cell lysates were then centrifuged at 800 rpm for 10 min at 4 °C. The supernatant containing the membrane was centrifuged again at 18,000 rpm for 30 min at 4 °C to collect the membrane pellets. Membrane pellets were resuspended in 2 mL of binding buffer containing 20 mM Tris pH 7.5, 100 mM NaCl, 100 μg/ml leupeptin, and 160 μg/ml benzamidine. The purified membrane was then aliquoted into 100 μL/tube, flash-frozen with liquid nitrogen, and stored at −80 °C before further use.

In the competition binding assay, the membrane suspension was diluted to appropriate concentration with binding buffer containing 20 mM Tris, pH 7.5, 100 mM NaCl, and 0.5 mg/mL BSA, and incubated with radioligand (1 nM ^{3}H prazosin or 2 nM ^{3}H DHA) as well as different concentration of AdTx1 or AdTx1 mutants or other cold ligands at room temperature.

After shaking at 150 rpm for 2 h at room temperature, the membrane was collected by filtration and washed 3–4 times with ice-cold binding buffer using a 96-well Brandel harvester. The membrane-containing filter paper was then incubated with solid scintillation mix for 5 min at 85 °C. Radioactivity results were counted by a Microbeta2 scintillation counter.

GloSensor cAMP assay

A GloSensor cAMP kit from Promega (Cat. No. E1291) was used in this study. In brief, the pGloSensor™-22F plasmid, receptor plasmid, and Gsq plasmid were transfected into HEK293T cells (ATCC). As mentioned earlier, the α_{1A}AR couples to Gq, which could not induce cAMP accumulation; thus, we used an engineered Gsq protein constructed by replacing 15 residues at the C-terminus of Gs with those of Gq. The Gsq protein could be activated by the α_{1A}AR and stimulate cAMP generation.

24 h after transfection, the cells were switched into CO_2-Independent Medium (Gibco). Generally, the cells from one well of a 6-well plate were resuspended in 8 mL medium, and incubated with 6 mg GloSensor™ cAMP Reagent. The mixture was then transferred to a 96-well plate with 80 μL of cell suspension per well. The 96-well plate is placed at 37 °C in the dark for 1 h, then placed at room temperature in the dark for 1 h before use.

The following procedures were performed at room temperature. To measure the inhibition profile of the toxin or toxin mutants, 10 μL of the diluted AdTx1 or AdTx1 mutants were added to the well plate. After 15 min of incubation, 10 μL of the small-molecule agonists (norepinephrine or oxymetazoline) were added to the system. The chemoluminescence signal was measured around 10–15 min after the addition of the agonist.

Statistics and reproducibility

The competition binding assay and Glosensor cAMP assay curves were presented as means ± SEM, and calculated and fitted by non-linear regression using GraphPad Prism 8. Statistical comparisons were performed by an additional sum of squares F-test, and $P < 0.05$ was considered statistically significant.

Reporting summary

Further information on research design is available in the Nature Portfolio Reporting Summary linked to this article.

Data availability

The coordinates of the AdTx1-α_{1A}AR-Nb6 structure have been deposited in the Protein Data Bank (PDB) under accession number 8HN1. The cryo-EM density map of the AdTx1-α_{1A}AR-Nb6 structure has been deposited in the Electron Microscopy Data Bank under accession code EMD-34906.

Received: 2 April 2023; Accepted: 17 June 2025;
Published online: 16 July 2025

References

1. Saikia, S., Bordoloi, M. & Sarmah, R. Established and In-trial GPCR Families in Clinical Trials: A Review for Target Selection. *Curr. Drug Targets* **20**, 522–539 (2019).
2. Kini, R. & Doley, R. Structure, function and evolution of three-finger toxins: mini proteins with multiple targets. *Toxicon* **56**, 855–867 (2010).
3. Utkin, Y. N. Animal venom studies: current benefits and future developments. *World J. Biol. Chem.* **6**, 28 (2015).
4. Ianzer, D. et al. Identification of five new bradykinin potentiating peptides (BPPs) from Bothrops jararaca crude venom by using electrospray ionization tandem mass spectrometry after a two-step liquid chromatography. *Peptides* **25**, 1085–1092 (2004).
5. Frangieh, J. et al. Snake venom components: tools and cures to target cardiovascular diseases. *Molecules* **26**, 2223 (2021).
6. Marcinkiewicz, C. Functional characteristic of snake venom disintegrins: potential therapeutic implication. *Curr. Pharm. Des.* **11**, 815–827 (2005).
7. Tcheng, J. E. & O'Shea, J. C. Eptifibatide: a potent inhibitor of the platelet receptor integrin glycoprotein IIb/IIIa. *Expert Opin. Pharmacother.* **3**, 1199–1210 (2002).
8. Sherman, D. G. Ancrod. *Curr. Med. Res. Opin.* **18**, S48 (2002).
9. Hannan, S., Mortensen, M. & Smart, T. G. Snake neurotoxin α-bungarotoxin is an antagonist at native GABAA receptors. *Neuropharmacology* **93**, 28–40 (2015).
10. Quik, M. & Geertsen, S. Neuronal nicotinic α-bungarotoxin sites. *Can. J. Physiol. Pharmacol.* **66**, 971–979 (1988).
11. Harel, M. et al. The binding site of acetylcholine receptor as visualized in the X-ray structure of a complex between α-bungarotoxin and a mimotope peptide. *Neuron* **32**, 265–275 (2001).
12. Quinton, L. et al. Isolation and pharmacological characterization of AdTx1, a natural peptide displaying specific insurmountable antagonism of the alpha1A-adrenoceptor. *Br. J. Pharmacol.* **159**, 316–325 (2010).
13. Maïga, A. et al. Orthosteric binding of ρ-Da1a, a natural peptide of snake venom interacting selectively with the α1A-adrenoceptor. *PLoS ONE* **8**, e68841 (2013).
14. Endo, T., Tamiya, N. & Harvey, A. Snake toxins. 165–222 (Pergamon Press, New-York, 1991).
15. Haenisch, B. et al. Alpha-adrenoceptor agonistic activity of oxymetazoline and xylometazoline. *Fundam. Clin. Pharmacol.* **24**, 729–739 (2010).
16. Roehrborn, C. G. & Schwinn, D. A. α1-Adrenergic receptors and their inhibitors in lower urinary tract symptoms and benign prostatic hyperplasia. *J. Urol.* **171**, 1029–1035 (2004).
17. Rossi, M. & Roumeguère, T. Silodosin in the treatment of benign prostatic hyperplasia. *Drug Des. Dev. Ther.* **4**, 291–297 (2010).

18. Fawzy, A. et al. Doxazosin in the treatment of benign prostatic hyperplasia in normotensive patients: a multicenter study. *J. Urol.* **154**, 105–109 (1995).
19. Fulton, B., Wagstaff, A. J. & Sorkin, E. M. Doxazosin. *Drugs* **49**, 295–320 (1995).
20. Green, B. Prazosin in the treatment of PTSD. *J. Psychiatr. Pract.* **20**, 253–259 (2014).
21. Toyoda, Y. et al. Structural basis of α1A-adrenergic receptor activation and recognition by an extracellular nanobody. *Nat. Commun.* **14**, 3655 (2023).
22. Maeda, S. et al. Structure and selectivity engineering of the M muscarinic receptor toxin complex. *Science* **369**, 161–167 (2020).
23. Nehmé, R. et al. Mini-G proteins: Novel tools for studying GPCRs in their active conformation. *PLoS ONE* **12**, e0175642 (2017).
24. Che, T. et al. Nanobody-enabled monitoring of kappa opioid receptor states. *Nat. Commun.* **11**, 1–12 (2020).
25. Robertson, M. J. et al. Structure determination of inactive-state GPCRs with a universal nanobody. *Nat. Struct. Mol. Biol*. https://doi.org/10.1038/s41594-022-00859-8 (2022).
26. Ballesteros, J. A. & Weinstein, H. in *Methods in Neurosciences* Vol. 25 366–428 (Elsevier, 1995).
27. Van Baelen, A.-C. et al. Structural and functional diversity of animal toxins interacting with GPCRs. *Front. Mol. Biosci.* **9**, 811365 (2022).
28. Shi, L. & Javitch, J. A. The binding site of aminergic G protein-coupled receptors: the transmembrane segments and second extracellular loop. *Annu. Rev. Pharmacol. Toxicol.* **42**, 437 (2002).
29. Surgand, J. S., Rodrigo, J., Kellenberger, E. & Rognan, D. A chemogenomic analysis of the transmembrane binding cavity of human G-protein-coupled receptors. *Proteins Struct. Funct. Bioinform.* **62**, 509–538 (2006).
30. Xu, X. et al. Binding pathway determines norepinephrine selectivity for the human β1AR over β2AR. *Cell Res.* **31**, 569–579 (2021).
31. Ring, A. M. et al. Adrenaline-activated structure of β2-adrenoceptor stabilized by an engineered nanobody. *Nature* **502**, 575–579 (2013).
32. Xu, P. et al. Structural insights into the lipid and ligand regulation of serotonin receptors. *Nature* **592**, 469–473 (2021).
33. Xiao, P. et al. Ligand recognition and allosteric regulation of DRD1-Gs signaling complexes. *Cell* **184**, 943–956.e918 (2021).
34. Im, D. et al. Structure of the dopamine D2 receptor in complex with the antipsychotic drug spiperone. *Nat. Commun.* **11**, 1–11 (2020).
35. Yasuda, S. et al. Hot-spot residues to be mutated common in G protein-coupled receptors of class A: identification of thermostabilizing mutations followed by determination of three-dimensional structures for two example receptors. *J. Phys. Chem. B* **121**, 6341–6350 (2017).
36. Lei, J. & Frank, J. Automated acquisition of cryo-electron micrographs for single particle reconstruction on an FEI Tecnai electron microscope. *J. Struct. Biol.* **150**, 69–80 (2005).
37. Zheng, S. Q. et al. MotionCor2: anisotropic correction of beam-induced motion for improved cryo-electron microscopy. *Nat. Methods* **14**, 331–332 (2017).
38. Punjani, A., Rubinstein, J. L., Fleet, D. J. & Brubaker, M. A. cryoSPARC: algorithms for rapid unsupervised cryo-EM structure determination. *Nat. Methods* **14**, 290–296 (2017).
39. Pettersen, E. F. et al. UCSF Chimera–a visualization system for exploratory research and analysis. *J. Comput Chem.* **25**, 1605–1612 (2004).
40. Afonine, P. V. et al. Real-space refinement in PHENIX for cryo-EM and crystallography. *Acta Crystallogr. Sect. D Struct. Biol.* **74**, 531–544 (2018).
41. Emsley, P. & Cowtan, K. Coot: model-building tools for molecular graphics. *Acta Crystallogr. Sect. D: Biol. Crystallogr.* **60**, 2126–2132 (2004).
42. Pettersen, E. F. et al. UCSF ChimeraX: structure visualization for researchers, educators, and developers. *Protein Sci.* **30**, 70–82 (2021).
43. Kruse, A. C. et al. Activation and allosteric modulation of a muscarinic acetylcholine receptor. *Nature* **504**, 101–106 (2013).
44. Swaminath, G., Steenhuis, J., Kobilka, B. & Lee, T. Allosteric modulation of beta2-adrenergic receptor by Zn(2+). *Mol. Pharmacol.* **61**, 65–72 (2002).

Acknowledgements

We are grateful for the support of the National Protein Science Research (Beijing) Facility, Tsinghua Base, and the Radioisotope Laboratory of the Center for Biomedical Analysis, Tsinghua University. This work was supported by Beijing Frontier Research Center for Biological Structure, Tsinghua University (M.S., S.Z., A.Z., Y.T., X.S., X.X., C.Y., and X.L.), Tsinghua University-Peking University Joint Center for Life Sciences (CLS) (C.Y. and X.L.), by Beijing Municipal Natural Science Foundation (Grant 5232008 to X.L.), National Natural Science Foundation of China (Grant 32122041 to X.L. and Grant 32100968 to X.X.), China Postdoctoral Science Foundation 2021M691809 (X.X.) and Tsinghua University Initiative Scientific Research Program (X.L.).

Author contributions

M.S. performed AdTx1, α_{1A}AR, and Nb6 expression, purification, and complex formation with help from Y.T., X.S., and X.X. S.Z., A.Z., and F.K. performed cryo-EM data processing and structure refinement. M.S. characterized the pharmacological properties of AdTx1 and mutants. S.Z. completed the preparation of cryo-EM samples, and A.Z. performed data collection and processing. C.Y. oversaw the cryo-EM data processing and structure refinement. X.L., X.S., and X.X. coordinated the experiments and oversaw the overall study. M.S., S.Z., and X.L. wrote the manuscript. All authors contributed to the editing of the paper.

Competing interests

The authors declare no competing interests.

Additional information

Supplementary information The online version contains supplementary material available at https://doi.org/10.1038/s42003-025-08405-0.

Correspondence and requests for materials should be addressed to Xiaoou Sun, Xinyu Xu, Chuangye Yan or Xiangyu Liu.

Peer review information *Communications Biology* thanks Richard Lewis, Nicolas Gilles, and the other anonymous reviewer for their contribution to the peer review of this work. Primary Handling Editors: Ross Bathgate and Laura Rodríguez Pérez.